Chemical Science

ROYAL SOCIETY OF CHEMISTRY

EDGE ARTICLE

View Article Online
View Journal | View Issue

Open Access Article. Published on 23 January 2025. Downloaded on 10/29/2025 1:09:32 AM.
This article is licensed under a Creative Commons Attribution-NonCommercial 3.0 Unported Licence.

Check for updates

Cite this: *Chem. Sci.*, 2025, **16**, 3536

All publication charges for this article have been paid for by the Royal Society of Chemistry

Efficient harvesting of triplet excitons *via* multiple fast TTA up-conversion and high-lying reverse intersystem crossing channels for efficient blue fluorescent organic light-emitting diodes†

Jianwen Qin, Xianfeng Qiao,* Shu Xiao, Dezhi Yang, Yanfeng Dai, Jiangshan Chen, Qian Sun and Dongge Ma*

Received 14th September 2024
Accepted 6th January 2025

DOI: 10.1039/d4sc06232a

rsc.li/chemical-science

The efficient harvesting of triplet excitons is key to realizing high efficiency blue fluorescent organic light-emitting diodes (OLEDs). Triplet–triplet annihilation (TTA) up-conversion is one of the effective triplet-harvesting strategies. However, during the TTA up-conversion process, a high current density is necessary due to the competitive non-radiative triplet losses. In this study, we designed blue organic light-emitting diodes with fast TTA up-conversion and high-lying reverse intersystem crossing channels. It can be seen that the utilization of triplet excitons was greatly improved and the non-radiative triplet losses were significantly suppressed due to the availability of multiple efficient channels for triplet exciton utilization. As a result, a high efficiency blue fluorescent OLED was successfully fabricated. The maximum external quantum efficiency (EQE) reached 11.4% with CIE coordinates of (0.13, 0.11). This research provides a new route for the development of high efficiency blue fluorescent OLEDs.

1. Introduction

Organic light emitting diodes (OLEDs) are attracting great interest for display and lighting applications.[1] Over the past three decades, high efficiency green and red phosphorescent OLEDs based on heavy metal complexes (generally Ir or Pt) have been applied in commercial products.[2,3] However, the phosphorescent OLEDs always exhibit serious efficiency roll-off at high current density caused by triplet–triplet annihilation (TTA) originating from the accumulation of long lifetime triplet excitons.[4] Whilst phosphorescent materials, which contain rare metals, for example, Ir, Pt, and Os, have a high cost of commercial production. Moreover, the development of blue phosphorescent OLEDs, especially those with deep-blue emissions, has lagged behind and hit a bottleneck.[5] To resolve the above problems, metal-free organic fluorescent emitters that efficiently utilize triplet excitons, for example, *via* triplet–triplet annihilation (TTA) up-conversion,[6,7] hybridized local and charge transfer (HLCT),[8] and thermally activated delayed fluorescence (TADF),[9,10] have been developed. Among them, TTA up-conversion emitters have shown fairly long operational lifetimes and low efficiency roll-off when used in OLEDs, which is an advantage over the phosphorescent emitters and TADF emitters.[11–17] Therefore, TTA up-conversion emitters have become promising candidates for blue fluorescent OLEDs. Polyacenes, such as anthracene, pyrene and tetracene derivatives, exhibit TTA up-conversion properties. Many TTA up-conversion molecules with anthracene and pyrene as the cores have been investigated[18–23] because anthracene and pyrene have suitable T_1 energy levels, thus making them able to undergo a TTA up-conversion process. However, the theoretical maximum radiative singlet-exciton ratio generated from the TTA process is known to be 15%. If considering the directly generated singlets of 25%, the total singlet excitons available for emission is not greater than 40%. Obviously, the contribution of TTA up-conversion to efficient emission is small. Thus, ways to further improve the contribution of TTA up-conversion to emission has become an important research topic. Friend *et al.* reported a 26–37% TTA contribution (delayed fluorescence contribution) to the total emission using DPA and perylene as a blue emitter.[7] Kim *et al.* reported a 41–48% TTA contribution to the total emission using a newly developed TTA material and a device structure containing an efficiency enhancement layer (EEL).[16,23] Kido *et al.* synthesized a deep blue TTA emitter with a double anthracene core, however, the devices made from this material had a severe EQE roll-off and no TTA contribution was present.[6] On the other hand, the high-lying reverse intersystem

Institute of Polymer Optoelectronic Materials and Devices, Guangdong Basic Research Center of Excellence for Energy & Information Polymer Materials, Guangdong-Hong Kong-Macao Joint Laboratory of Optoelectronic and Magnetic Functional Materials, Guangdong Provincial Key Laboratory of Luminescence from Molecular Aggregates, State Key Laboratory of Luminescent Materials and Devices, South China University of Technology, Guangzhou 510640, China. E-mail: msxqiao@scut.edu.cn; msdgma@scut.edu.cn

† Electronic supplementary information (ESI) available. See DOI: https://doi.org/10.1039/d4sc06232a

© 2025 The Author(s). Published by the Royal Society of Chemistry

Open Access Article. Published on 23 January 2025. Downloaded on 10/29/2025 1:09:32 AM.
This article is licensed under a Creative Commons Attribution-NonCommercial 3.0 Unported Licence.

crossing (hRISC) process is another rapid triplet exciton conversion channel, which occurs from high-lying triplet states (T_n, $n \geq 2$) to singlet states (S_m, $m \geq 1$). The internal conversion (IC) process from the T_n to T_1 states should be suppressed to guarantee the utilization of triplet excitons. Recently, some HLCT materials with a fast hRISC process have been investigated.[24–26] Nevertheless, to date, the reports on HLCT materials discuss few TTA features, which is not beneficial for the utilization of triplet excitons.

In this study, we developed a blue organic emitter with a fast TTA up-conversion process and high-lying reverse intersystem crossing features. It can be seen that the availability of multiple efficient channels significantly improved the utilization of the triplet excitons, thus greatly enhancing the efficiency of the resulting blue fluorescent OLEDs. The maximum external quantum efficiency EQE_{max} reached 11.4% with CIE coordinates of (0.13, 0.11).

2. Results and discussions

In the case of TTA up-conversion with high-lying reverse intersystem crossing channels, as illustrated in Fig. 1a, the TTA up-conversion process involves two steps: (1) two low-energy triplets collide and form a spin-correlative triplet–triplet (TT) pair, and then (2) the interacting TT pair converts into a high-energy excited state and a ground state. In the first step, the TT pair will consist of nine spin states, which contain one singlet-featuring state ^{1}(TT), three triplet-featuring states ^{3}(TT), and five quintet (Q)-featuring states ^{5}(TT). In the second step, the ^{1}(TT), ^{3}(TT) and ^{5}(TT) states convert into a high-energy singlet state (S_m). Although the internal quantum efficiency (IQE) can theoretically reach 62.5%, it is actually only 40%, corresponding to a maximum EQE of 8%. If there simultaneously exists an efficient high-lying reverse intersystem crossing (hRISC) process from the T_n ($n \geq 2$) to singlet state S_m ($m \geq 1$) which is fast enough to compete with the TTA up-conversion process, then theoretically the IQE may reach 100%. However, the IQE is greatly reduced due to the existence of internal conversion (IC) from T_n to T_1, and thus there is a lack of effective conversion from triplets to singlets, which is non-radiative triplet decay (Fig. 1b). Obviously, to realize an efficient triplet harvesting process, fast rates of hRISC and TTA up-conversion are necessary to restrain the undesired internal conversion and non-radiative triplet decay channels. To trigger a rapid and efficient hRISC process, an ultra-small energy level difference between S_m and T_n ($\Delta E_{S_m \to T_n}$) and a relatively large spin–orbit coupling matrix element (SOCME) between the T_n and S_m states are necessary. Additionally, a sufficiently large energy gap between the T_n and T_1 states is favorable to attain a slow rate of internal conversion from T_n to T_1. Therefore, the design of molecules with fast rates of TTA and hRISC are desirable.

Here, a new highly efficient blue-emitting material, PyAnCN, containing anthracene and pyrene units with fast TTA and HLCT processes was synthesized (Fig. 2a). The synthetic route to obtain PyAnCN is shown in Scheme S1.† The chemical structure of PyAnCN was well characterized using NMR, and mass spectroscopy (MS). The absorption bands of PyAnCN at 377 and 397 nm are characteristics of the π–π* transition of the

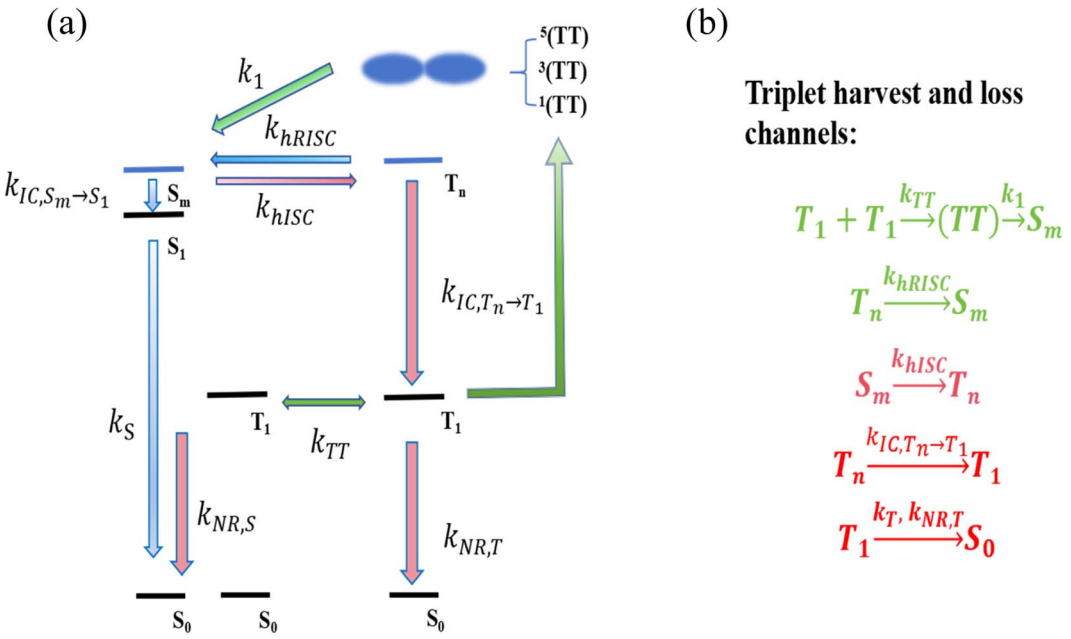

Fig. 1 Possible exciton processes in TTA–HLCT molecules. (a) Energy-level diagram illustrating the mechanism of TTA–HLCT. (b) Triplet harvest and loss channels in the TTA–HLCT processes. ^{1}(TT), ^{3}(TT) and ^{5}(TT) are the singlet-, triplet-, and quintet-featuring (TT) intermediate states, respectively. S_1, T_1, and S_0 are the lowest excited singlet state, the lowest excited triplet state and ground state, respectively. S_m is the higher-lying singlet state, and T_n is the higher-lying triplet state. k_1 is the rate constant for the conversion of the TT pairs into singlets. k_S is the rate constant of singlet radiative decay. $k_{NR,S}$ and $k_{NR,T}$ are the rate constants of singlet and triplet non-radiative decay, respectively. $k_{IC,S_m \to S_1}$ and $k_{IC,T_n \to T_1}$ are the rate constants of the internal conversion (IC) processes from S_m to S_1 and from T_n to T_1, respectively.

Open Access Article. Published on 23 January 2025. Downloaded on 10/29/2025 1:09:32 AM.
This article is licensed under a Creative Commons Attribution-NonCommercial 3.0 Unported Licence.

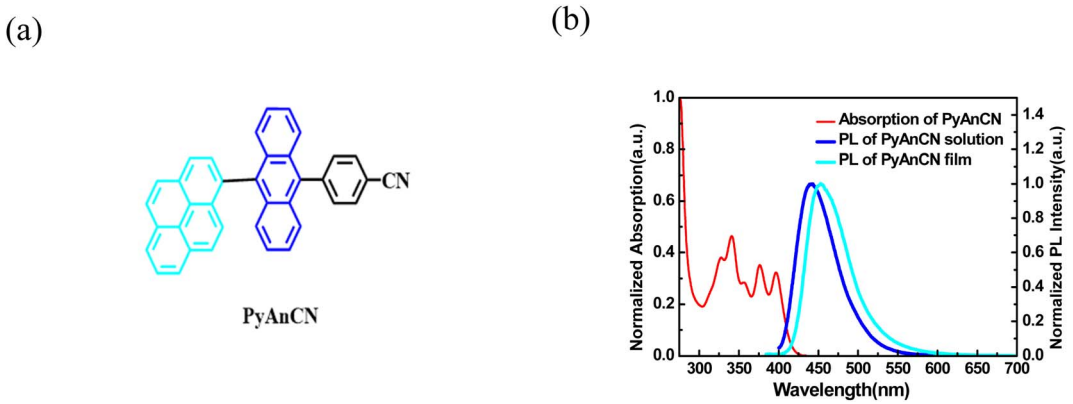

Fig. 2 (a) Molecular structure of PyAnCN. (b) Absorption spectrum of PyAnCN in toluene solution (10^{-5} M), PL emission spectra of a PyAnCN solution and neat film.

anthracene moiety. The PL spectrum of PyAnCN shows a deep blue emission, and the emission peak shifts from 443 nm in solution to 454 nm in a neat film (Fig. 2b). As displayed in Fig. S1,† PyAnCN in toluene shows monoexponential decay, and thus the radiative decay constant (k_S) of the S_1 state can be estimated. A neat PyAnCN film with encapsulation shows multi-exponential decay, and thus may exhibit more up-conversion processes. The photophysical properties of PyAnCN are provided in Table 1. The phosphorescence of PyAnCN was recorded at 77 K in glassy toluene using PtOEP as a sensitizer. As displayed in Fig. S2,† PtOEP is pumped to its excited state, followed by a fast energy transfer to the T_1 state of PyAnCN. With a delay of 1 ms, the phosphorescence of PyAnCN can be detected. The first vibrational peak of the phosphorescence is at 704 nm, corresponding to a T_1 energy of 1.73 eV. In order to validate the TTA up-conversion characteristics of PyAnCN, we conducted experiments on PyAnCN sensitized by PtOEP. As shown in Fig. S3,† two different linear regimes are obtained when a curve of up-conversion intensity with incident power is plotted. At low excitation power, the TTA up-conversion becomes negligible with respect to spontaneous PyAnCN non-radiative decay, which is the main triplet deactivation channel. In this case, the region can be well fitted with a straight line with a slope of 1.73. At high excitation power, the TTA up-conversion becomes dominant, and the PL intensity becomes proportional to the excitation power density with a slope of 1.18, which is consist with TTA up-conversion kinetics in a multi-component system model under steady-state conditions. To further demonstrate the excited state properties of PyAnCN, the natural transition orbitals (NTOs) were calculated using the TD-B3LYP/6-31G(d) method based on the optimized S_1 geometry. As shown in Fig. S4,† the NTOs of the T_1 energy state in PyAnCN are as low as 1.8 eV, arising from the long conjugation axis of anthracene, which is in good accordance with the experimental measurements. The T_2 energy in PyAnCN is as low as 2.0 eV, which arises from the long conjugation axis of pyrene. To utilize PyAnCN as a blue emitter in OLEDs, we fabricated non-doped OLEDs with a device structure of indium tin oxide (ITO)/HATCN (15 nm)/TAPC (55 nm)/TCTA (10 nm)/PyAnCN (20 nm)/TPBi (40 nm)/LiF (1 nm)/Al (120 nm). HAT-CN and LiF were used as the hole and electron injection layers, respectively. TAPC and TPBi were used as the hole and electron transporting layers, respectively, and TCTA acted as the electron blocking layer. The energy level diagram of the device and the chemical structures of the used materials are also shown in Fig. S5.† The EL spectrum shows an emission peak of 450 nm with CIE coordinates of (0.15, 0.11) at 6 V. The maximum current efficiency reaches 5.9 cd A^{-1} (Table S1†). The maximum EQE is as high as 5.9% at a high luminescence of 1000 cd m^{-2}. To verify the possibility of using PyAnCN as a host, we further fabricated blue OLEDs based on an emitter made from a multiple resonance (MR) induced material with a narrow full-width at half-maximum (FWHM) in a rigid core structure, as this shows a better color purity.[27–32] The investigated device structure was ITO/HAT-CN (15 nm)/TAPC (55 nm)/TCTA (10 nm)/emitter (20 nm)/TPBi (40 nm)/LiF (1 nm)/Al (100 nm), where the emitter was PyAnCN : 3% TBN-TPA.[33] As shown in Fig. S6,† an effective Förster energy transfer between PyAnCN and TBN-TPA exists due to their large spectral overlap. The optimized device with a PyAnCN host displays an external quantum efficiency (EQE) of 9.1% with

Table 1 Photophysical data of PyAnCN

Compound	Abs_{sol}[a] [nm]	PL_{sol}[a] [nm]	PL_{film}[b] [nm]	HOMO/LUMO[c] [eV]	E_g[d] [eV]	Φ_{PL}[e] (%)
PyAnCN	341, 377, 396	443	454	−5.06/−2.06	3.0	57[f]/35[g]/54[h]

[a] Absorption and fluorescence spectra were measured in toluene solution at 10^{-5} M. [b] Measured as a neat film. [c] HOMO values were determined using the oxidative potentials of the materials with Fc/Fc^+ as the reference. LUMO levels were estimated according to the equation, LUMO = HOMO − E_g. [d] The energy gap (E_g) was estimated from the absorption threshold. [e] PL quantum yields of the emitters were obtained using an integral sphere with an excitation wavelength of 330 nm. [f] PLQY in dilute toluene (10^{-5}). [g] PLQY of the neat film. [h] PLQY of the doped film (10% in mCBP).

 © 2025 The Author(s). Published by the Royal Society of Chemistry

Open Access Article. Published on 23 January 2025. Downloaded on 10/29/2025 1:09:32 AM.
This article is licensed under a Creative Commons Attribution-NonCommercial 3.0 Unported Licence.

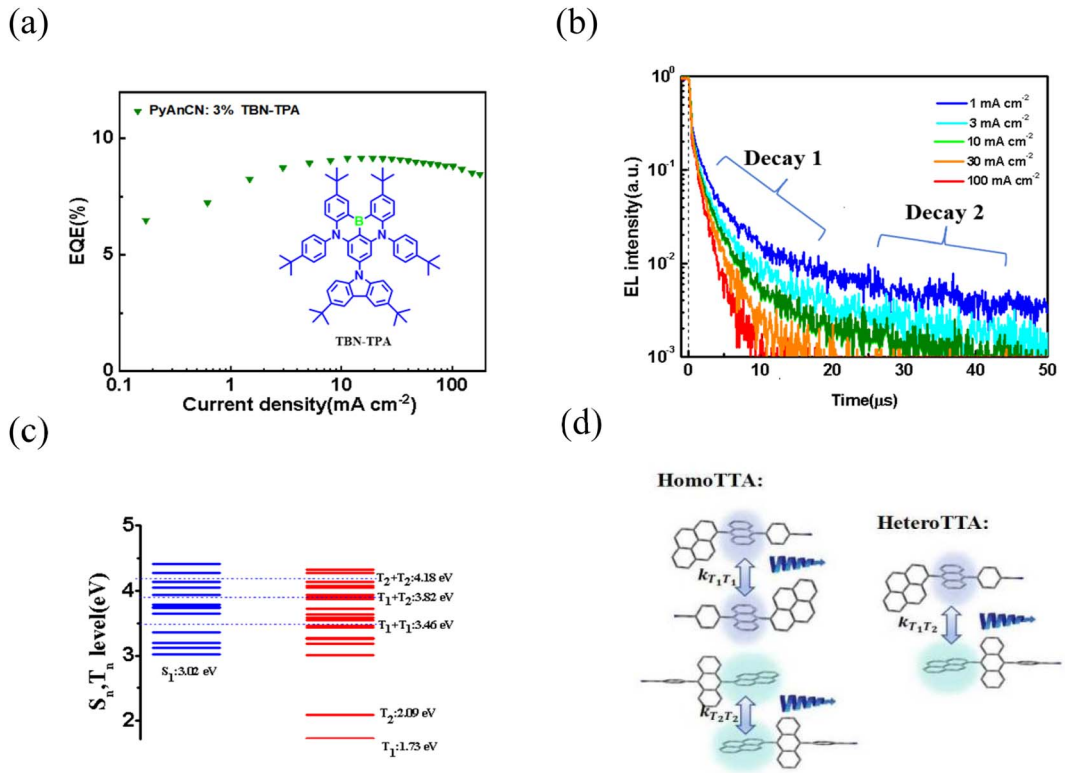

Fig. 3 (a) EQE-current density characteristics of the PyAnCN host-based OLED (inset: molecular structure of TBN-TPA). (b) Transient EL decay curves of the PyAnCN host-based OLED at different current densities. (c) Energy landscape for the singlet and triplet excited states of PyAnCN. (d) Possible electron cloud interaction of PyAnCN at different TTA rates.

a small efficiency roll-off (Fig. 3a). To understand the exciton behavior, the transient EL characteristics of the device were investigated, and the results are presented in Fig. 3b. The transient EL characteristics of the doped device show almost the same current density dependent trend. Given that TTA up-conversion is essentially a bimolecular process, the luminance–current density (*L*–*J*) curve of the device was plotted in double-log form, and the slopes of the corresponding fitted lines were calculated. As shown in Fig. S7,† under the excitation intensity conditions of $J = 0.5$ mA cm^{-2}, the fitted line is almost linearly dependent. The EL decay in the double-log form can be linearly fitted with a slope of −1.9 at a time range of 2–20 μs, which fits well with the TTA up-conversion model expressed as follows:

$$\frac{\mathrm{d}[T(t)]}{\mathrm{d}t} = -k_{\mathrm{NR,T}}[T(t)] - k_{\mathrm{TT}}[T(t)]^2 \quad (1)$$

where $T(t)$ is the T_1 density, $k_{\mathrm{NR,T}}$ is the rate of non-radiative triplet decay, and k_{TT} is the overall rate constant of TTA up-conversion.

Under high exciton density conditions ($k_{\mathrm{TT}}[T(t)]^2 \gg k_{\mathrm{NR,T}}[T(t)]$), the solution of eqn (1) becomes

$$I_{\mathrm{DF}} \propto [T(t)]^2 = \left(k_{\mathrm{TT}}t + \frac{1}{T(0)}\right)^{-2} = \frac{1}{(At+B)^2} \quad (2)$$

where I_{DF} is the intensity of the delayed EL induced by TTA up-conversion dominated processes, which should be the TTA up-conversion process that is responsible for the observed delayed EL emission in the device. The delayed emission showed a high delayed emission ratio of 31% at 3 mA cm^{-2} (Table S2†). As the current density increases, the device exhibits an ascending delayed emission ratio and the largest value (∼38%) is obtained when a pulse intensity of 100 mA cm^{-2} is applied. When the TTA up-conversion process occurs, at low current density, the delayed emission ratio (R_{d}) can be expressed as follows (see ESI steady-state kinetic eqn (1)–(9) for details†).

$$R_{\mathrm{d}} = \frac{\mathrm{EL_T}}{\mathrm{EL_S} + \mathrm{EL_T}} = \frac{f_1 k_{\mathrm{TT}}(1-P_{\mathrm{s}})^2 J}{f_1 k_{\mathrm{TT}}(1-P_{\mathrm{s}})^2 J + 2k_{\mathrm{NR,T}}{}^2 q d P_{\mathrm{s}}} \quad (3)$$

Here, P_{s} is the ratio of the excitons converted to singlets, q is the elementary charge, and d is the width of the recombination zone. f_1 represents the ratio of TTA up-conversion to singlets, and J is the current density. The TTA up-conversion saturation current density can be expressed as follows.

$$J_{\mathrm{TTA}} = \frac{k_{\mathrm{NR,T}}{}^2 q d}{k_{\mathrm{TT}}(1-P_{\mathrm{s}})} \quad (4)$$

The device with a PyAnCN host shows a small TTA up-conversion saturation current density, and thus the rate constant of TTA up-conversion (k_{TT}) and the rate of non-radiative triplet decay ($k_{\mathrm{NR,T}}$) can be calculated. The device with a PyAnCN host displays a fast rate constant of $k_{\mathrm{TT}} \sim 4.1 \times$

Open Access Article. Published on 23 January 2025. Downloaded on 10/29/2025 1:09:32 AM.
This article is licensed under a Creative Commons Attribution-NonCommercial 3.0 Unported Licence.

10^{-14} cm^3 s^{-1} for TTA up-conversion, and a slow rate of $k_{NR,T} \sim 3.4 \times 10^4$ s^{-1} for non-radiative triplet decay. The EL decay curve of the device with a PyAnCN host exhibits obvious two decays, which may contain more than one TTA up-conversion process. Fig. 3c and Table S3† display the energy levels of PyAnCN calculated at the level of B3LYP/6-31G(d) theory. Higher energy can be achieved through collisions and annihilation between the T_1 and T_1, T_1 and T_2, T_2 and T_2 states. Because of the low diffusion rate of the triplet excitons, the triplet excitons form TT pairs on the anthracene and pyrene groups adjacent to the molecule. ^{3}(TT) and ^{5}(TT) can convert quickly into a high-energy singlet state (S_m) through more degenerate channels. So, in this TTA up-conversion process, three TTA up-conversion channels (containing intramolecular TTA and intermolecular TTA) will be formed with spin-correlative triplet–triplet (TT) pairs. These channels may accelerate the TTA up-conversion process and reduce the non-radiative transitions (Fig. 3d). The multiple TTA up-conversion channels present mean that the transient EL decay curve of the device with a PyAnCN host exhibits two decays and more complex up-conversion processes.

Furthermore, the high-lying reverse intersystem crossing (hRISC) channel was investigated in the devices. The transient PL properties of the host : 3% TBN-TPA films were measured to reveal the high-lying reverse intersystem crossing (hRISC) processes, as shown in Fig. 4. It can be seen that the decay curves of the films show two decay components, which can be well fitted by a double exponential decay function. For a more intuitive analysis, the rate constants were calculated according to the photophysical equations and the detailed results are shown in Tables S4 and S5.† It is seen that the PyAnCN : 3% TBN-TPA film presents two lifetimes, 3.1 and 29.5 ns, corresponding to the prompt and delayed lifetimes, respectively, with a large decay ratio. The MADN : 3% TBN-TPA film presents also two lifetimes, 3.9 and 51 ns, for the prompt and delayed lifetimes, respectively, with a small decay ratio. Here, the large decay ratio (48.5%) is considered to be related to the fast $T_n \rightarrow S_m$ hRISC process (5.1×10^7 s^{-1} for PyAnCN), and the small decay ratio (13.8%) is considered to be related to the slow $T_n \rightarrow S_m$ hRISC process (0.9×10^7 s^{-1} for MADN). To gain insight into the hRISC process between the high-lying T_n and S_m states in the hosts, the electronic transition features of the T_n and S_m states were calculated (Fig. S8†). The slow rates of hISC and hRISC in the MADN host indicates that few triplet energy levels are close to the excited singlet energy levels, which is consistent with the calculated results. On the other hand, more triplet energy levels are close to the excited singlet energy levels in the PyAnCN host, and the degenerate triplet energy levels may accelerate the intersystem crossing and reverse intersystem crossing processes. Moreover, relatively large spin–orbit coupling matrix element (SOCME) values between the T_n and S_m states in PyAnCN were calculated (Table S6†). PyAnCN has a higher SOCME value ($\langle S_1|\hat{H}_{SOC}|T_5\rangle = 0.2616$ cm^{-1}) than MADN ($\langle S_1|\hat{H}_{SOC}|T_4\rangle = 0.10$ cm^{-1}),[34] and the large value of SOCME in PyAnCN accelerates the hISC and hRISC processes. The

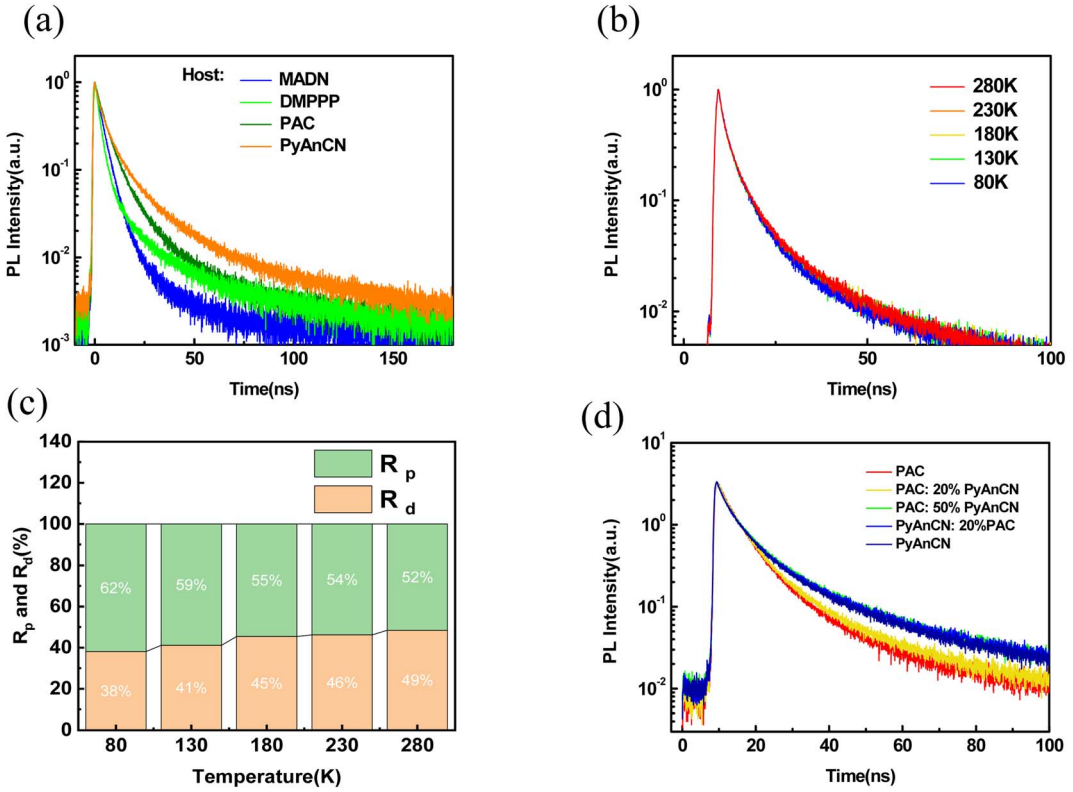

Fig. 4 (a) PL decay curves of the host : 3% TBN-TPA films at room temperature in O_2-free conditions. (b) PL decay curves of the PyAnCN : 3% TBN-TPA film at different temperatures. (c) The temperature-dependent prompt and delayed emission ratio of the PyAnCN : 3% TBN-TPA based OLEDs. (d) PL decay curves of the PAC : PyAnCN : 3% TBN-TPA films with different host concentrations.

 © 2025 The Author(s). Published by the Royal Society of Chemistry

Open Access Article. Published on 23 January 2025. Downloaded on 10/29/2025 1:09:32 AM. This article is licensed under a Creative Commons Attribution-NonCommercial 3.0 Unported Licence.

temperature-dependent transient PL decay characteristics of PyAnCN are shown in Fig. 4b. The prompt and decay lifetimes show no obvious change as the temperature increases. The delayed component increases monotonically as the temperature increases because hRISC becomes the rate-determining step. The results calculated for k_{hRISC} are consist with the activation energy from $\exp(-\Delta E_{ST}/k_B T)$, where k_B is the Boltzmann constant and T is the temperature (Table S7†). For comparison, the transient PL decay of the PAC : 3% TBN-TPA film exhibits a moderate k_{hRISC}. When the transient PL properties of the PAC : x% PyAnCN : 3% TBN-TPA films were measured, it was found that the k_{hRISC} of the PAC : 20% PyAnCN : 3% TBN-TPA film shows a higher decay ratio and faster hRISC rate than the PAC : 3% TBN-TPA films. When the PyAnCN doping concentration increases, the multi-component films show nearly the same decay ratio and PyAnCN dominates the hRISC process (Table S8†). The EL performances of the devices with different hosts are shown in Fig. S9 and Table S9.† High EQE deep blue OLEDs were achieved with small efficiency roll-off. Combined with the fast rate of TTA up-conversion in PyAnCN and the fast rate of hRISC in PAC, the PAC : 50% PyAnCN device displays an EQE of 10.3%, representing a further improvement. The transient EL characteristics were tested to further reveal the rate of TTA up-conversion and triplet non-radiative decay in the hosts (Fig. S10†). It is found that all hosts exhibit TTA up-conversion character with current density-dependent decay times and ratios. By fitting the EL decays, as shown, the host containing PyAnCN shows a large delayed emission ratio (Table S10†). The k_{TT}, $k_{NR,T}$, k_{hISC} and k_{hRISC} values of the hRISC and hISC processes were calculated using a previous model (Table S11†). It can be seen that the PAC : 50% PyAnCN host shows high rates of TTA up-conversion and hRISC due to its TTA–HCLT character (Table 2).

The working processes in the PAC : 50% PyAnCN : 3%-based OLEDs are presented in Fig. 5a. The multiple TTA up-conversion and high-lying reverse intersystem crossing channels should be dominant in these devices. In the resulting blue OLEDs, electrons and holes encounter and recombine simultaneously on the PAC and PyAnCN hosts during EML. The singlets on the host will convert to singlets of dopant with a fast Förster energy transfer rate. The triplets on the PAC : 50% PyAnCN host can convert into singlets with a fast high-lying reverse intersystem crossing channel and the more effective TTA up-conversion channel of PyAnCN due to the faster rate of TTA up-conversion. In this triplet harvesting channel, the triplet losses (internal conversion and triplet non-radiative decay) are well suppressed. The PAC : 50% PyAnCN-based device combines the excellent TTA up-conversion and hRISC of PyAnCN and the carrier transport characteristics of PAC, thus achieving better EL device performance. Moreover, the deep blue dopant M-tDABNA and low refractive index ETL B3PyMPM were adopted to further optimize the device performance.[35] The PAC : 50% PyAnCN-based device exhibits a deep blue color with CIE coordinates of (0.13, 0.11) and the EQE_{max} reaches 11.4% with a low efficiency roll-off of 11.3% at a luminance of 1000 cd m^{-2}, which remains 10.7% even at a luminance of 5000 cd m^{-2}. The EQE represents one of the best values among blue fluorescent OLEDs based on TTA/HLCT hosts (Fig. S11†). The higher EQE may also originate from the higher emitting dipole orientation of the emitting dopant. The horizontal dipole orientation ratio of PAC : 50% PyAnCN : 3% M-tDABNA was measured to be as high as 0.90 (Fig. 5c). The fast rates of hRISC and TTA up-conversion restrain the undesired internal conversion and non-radiative triplet decay channels, thus realizing an efficient triplet harvesting process. The transient EL measurement results are presented in Fig. 5d. Benefiting from a large k_{TTA}, the EL decay in the PAC : 50% PyAnCN-based device exhibits a high decay ratio at low current density. The ratio of the delayed emission exceeds 40% at a pulse current density of 30 mA cm^{-2} demonstrating the effective conversion of triplets to singlets by a more effective strategy, thus suppressing harmful triplet–polaron annihilation (TPA) and other exciton annihilation processes. To attain hRISC and TTA contributions, the EQEs of the devices were calculated and the relative contribution of all the relevant mechanisms of the exciton losses are plotted in Fig. S12,† assuming charge balance in the devices. At lower current densities, the dominating deactivation process for triplet states is non-radiative triplet decay, suggesting that a large number of triplets become deactivated during the triplet decay process. With increasing current density, the area corresponding to TTA up-conversion gradually increases and the TTA loss mechanism starts to dominate. The contribution of HLCT decreases from 16% to 9% with increasing current density, and the contribution of TTA increases from 6% to 14% in the PyAnCN-based OLED. It is clear that the HLCT significantly contributes to the fluorescence emission in the PAC : 50% PyAnCN-based device, and the HLCT ratio rises from 16% to 19% compared with the PyAnCN-based device at 1 mA cm^{-2}. With increasing current density, the area corresponding to HCLT gradually decreases, indicating that TTA up-conversion and HCLT compete with each other and TTA becomes dominant after the triplet exciton population increases. Devices based on the PyAnCN and PAC : 50% PyAnCN hosts were fabricated for an extended lifetime, and the lifetime of the devices were nearly doubled compared to that of the MADN host device (Fig. S13†). We believe that our work will attract

Table 2 EL performance of the optimized device

EML	V_{on}[a] (V)	L_{max}[b] (cd m^{-2})	CE_{max}/CE_{1000}[c] (cd A^{-1})	EQE_{max}/EQE_{1000}[d] (%)	EL_{max}[e] (nm)	CIE[f] (x, y)
PAC : 50% PyAnCN : 3% M-tDABNA	3.6	11 370	10.3/10.2	11.4/11.3	462	(0.13, 0.11)

[a] V_{on}: turn-on voltage at a luminescence of 1 cd m^{-2}. [b] L_{max}: maximum luminescence. [c] CE_{max}: maximum current efficiency. [d] EQE_{max}/EQE_{1000}: EQE maximum/at 1000 cd m^{-2}. [e] EL_{max}: emission peak of EL spectrum at 6 V. [f] CIE coordinates at 6 V.

Open Access Article. Published on 23 January 2025. Downloaded on 10/29/2025 1:09:32 AM.
This article is licensed under a Creative Commons Attribution-NonCommercial 3.0 Unported Licence.

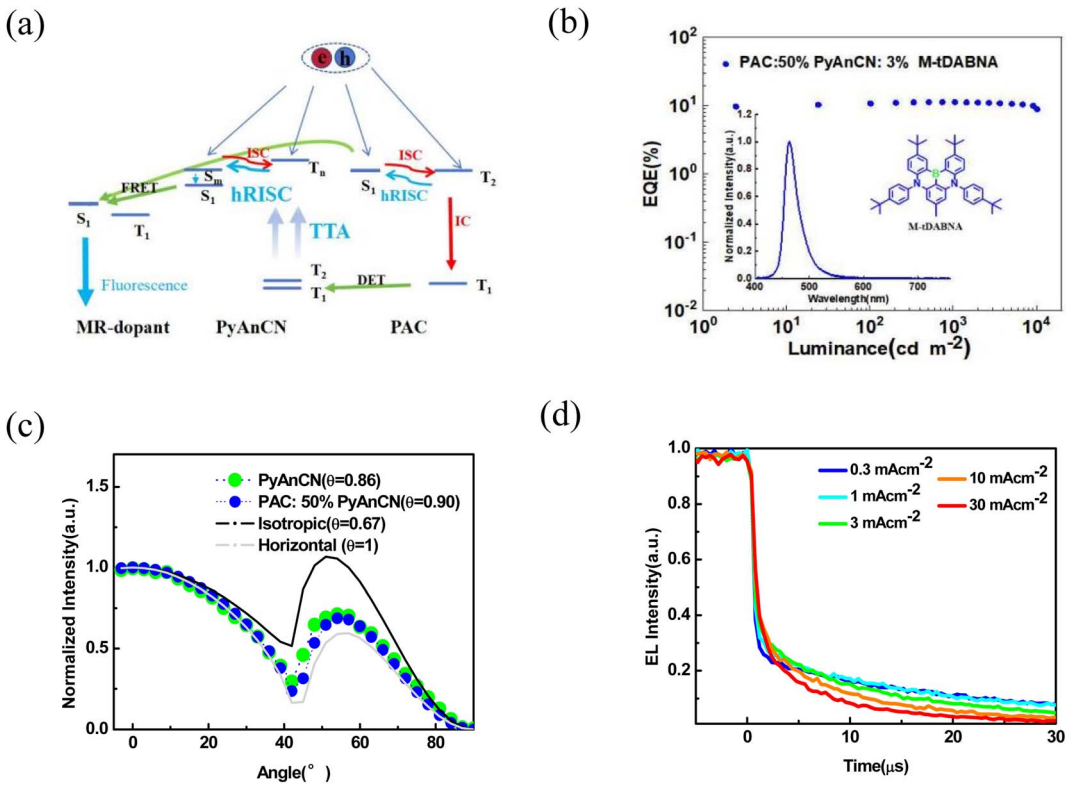

Fig. 5 (a) The working processes in the PAC : 50% PyAnCN : 3%-based OLEDs. (b) EQE *versus* luminance for the PAC : PyAnCN : 3% M-tDABNA based OLEDs (inset: molecular structure of M-tDABNA and the EL spectrum). (c) Variable-angle PL profiles of the PyAnCN : 3% M-tDABNA and PAC : 50% PyAnCN : 3% M-tDABNA films. (d) Transient EL decay curves of the PAC : 50% PyAnCN : 3% M-tDABNA based OLEDs at different current densities.

researchers in this field to find more strategies to increase the rate of TTA and hRISC, which will lead to the commercialization of deep-blue OLEDs that break through efficiency limits.

3. Conclusion

Deep-blue fluorescent OLEDs based on a newly designed organic emitter with a fast TTA up-conversion and high-lying reverse intersystem crossing channels were developed, and the maximum EQE was improved to 11.4%. It was found that highly efficient triplet harvesting was realized due to the fast TTA up-conversion and HLCT channels. A theoretical model explains the experimental results and clearly demonstrates that the TTA contribution with a fast TTA up-conversion rate reached saturation at low current density. With fast TTA up-conversion and high-lying reverse intersystem crossing channels, the utilization of triplet excitons was greatly improved and the non-radiative triplet losses were significantly suppressed. These findings will create new opportunities for the development of high-efficiency deep-blue OLEDs.

Data availability

The data supporting this article have been included as part of the ESI.†

Author contributions

All authors contributed to the data analysis, discussion and revision of the manuscript. Jianwen Qin designed and synthesized the molecules and contributed to the solution photophysics, electrochemistry and density-functional theory calculations. Jianwen Qin and Shu Xiao fabricated and measured the OLEDs and performed the majority of the solid-state photophysics. Jianwen Qin and Dongge Ma wrote the manuscript. Xianfeng Qiao and Dongge Ma coordinated the project. Dezhi Yang, Yanfeng Dai, Jiangshan Chen and Qian Sun contributed to the data analysis. Dongge Ma supervised and conceived the research.

Conflicts of interest

There are no conflicts to declare.

Acknowledgements

The authors gratefully acknowledge the support by the National Key R&D Program of China (2022YFA1204404), and the Guangdong Provincial Key Laboratory of Luminescence from Molecular Aggregates, China (2019B030301003).

 © 2025 The Author(s). Published by the Royal Society of Chemistry

Open Access Article. Published on 23 January 2025. Downloaded on 10/29/2025 1:09:32 AM.
This article is licensed under a Creative Commons Attribution-NonCommercial 3.0 Unported Licence.

References

1 (*a*) Y. Im, S. Y. Byun, J. H. Kim, D. R. Lee, C. S. Oh, K. S. Yook and J. Y. Lee, *Adv. Funct. Mater.*, 2017, **27**, 1603007; (*b*) P. Keerthika and R. K. Konidena, *Adv. Opt. Mater.*, 2023, **11**, 2301732; (*c*) J. Y. Woo, M. H. Park, S. H. Jeong, Y. H. Kim, B. Kim, T. W. Lee and T. H. Han, *Adv. Funct. Mater.*, 2023, **35**, 2207454.

2 (*a*) X. Yang, G. Zhou and W. Y. Wong, *Chem. Soc. Rev.*, 2015, **44**, 8484–8575; (*b*) C. Poriel and J. Rault-Berthelot, *Adv. Funct. Mater.*, 2021, **31**, 2010547.

3 (*a*) B. Minaev, G. Baryshnikov and H. Agren, *Phys. Chem. Chem. Phys.*, 2014, **16**, 1719–1758; (*b*) M. Idris, S. C. Kapper, A. C. Tadle, T. Batagoda, D. S. Muthiah Ravinson, O. Abimbola, P. I. Djurovich, J. Kim, C. Coburn, S. R. Forrest and M. E. Thompson, *Adv. Opt. Mater.*, 2021, **9**, 2001994.

4 Q. Wang, J. Ding, D. Ma, Y. Cheng, L. Wang and F. Wang, *Adv. Mater.*, 2009, **21**, 2397–2401.

5 (*a*) L.-K. Li, M.-C. Tang, S.-L. Lai, M. Ng, W.-K. Kwok, M.-Y. Chan and V. W.-W. Yam, *Nat. Photonics*, 2019, **13**, 185–191; (*b*) J. Song, H. Lee, E. G. Jeong, K. C. Choi and S. Yoo, *Adv. Mater.*, 2020, **32**, 1907539.

6 J.-Y. Hu, Y.-J. Pu, F. Satoh, S. Kawata, H. Katagiri, H. Sasabe and J. Kido, *Adv. Funct. Mater.*, 2014, **24**, 2064–2071.

7 D. Di, L. Yang, J. M. Richter, L. Meraldi, R. M. Altamimi, A. Y. Alyamani, D. Credgington, K. P. Musselman, J. L. MacManus-Driscoll and R. H. Friend, *Adv. Mater.*, 2017, **29**, 1605987.

8 S. Zhang, L. Yao, Q. Peng, W. Li, Y. Pan, R. Xiao, Y. Gao, C. Gu, Z. Wang, P. Lu, F. Li, S. Su, B. Yang and Y. Ma, *Adv. Funct. Mater.*, 2015, **25**, 1755–1762.

9 (*a*) H. Uoyama, K. Goushi, K. Shizu, H. Nomura and C. Adachi, *Nature*, 2012, **492**, 234–238; (*b*) N. Li, F. Ni, X. Lv, Z. Huang, X. Cao and C. Yang, *Adv. Opt. Mater.*, 2021, **10**, 2101343.

10 Z. Yang, Z. Mao, Z. Xie, Y. Zhang, S. Liu, J. Zhao, J. Xu, Z. Chi and M. P. Aldred, *Chem. Soc. Rev.*, 2017, **46**, 915–1016.

11 X. Qiao and D. Ma, *Mater. Sci. Eng., R*, 2020, **139**, 100519.

12 A. Monguzzi, J. Mezyk, F. Scotognella, R. Tubino and F. Meinardi, *Phys. Rev. B:Condens. Matter Mater. Phys.*, 2008, **78**, 195112.

13 D. Y. Kondakov, *J. Soc. Inf. Disp.*, 2009, **17**, 137.

14 C. Ye, L. Zhou, X. Wang and Z. Liang, *Phys. Chem. Chem. Phys.*, 2016, **18**, 10818–10835.

15 X. Guo, Y. Liu, Q. Chen, D. Zhao and Y. Ma, *Adv. Opt. Mater.*, 2018, **6**, 1700981.

16 H. Lim, S. J. Woo, Y. H. Ha, Y. H. Kim and J. J. Kim, *Adv. Mater.*, 2022, **34**, e2100161.

17 S. Xiao, X. Qiao, C. Lin, L. Chen, R. Guo, P. Lu, L. Wang and D. Ma, *Adv. Opt. Mater.*, 2022, **10**, 2102333.

18 H. Jung, S. Kang, H. Lee, Y. J. Yu, J. H. Jeong, J. Song, Y. Jeon and J. Park, *ACS Appl. Mater. Interfaces*, 2018, **10**, 30022–30028.

19 W. Liu, S. Ying, R. Guo, X. Qiao, P. Leng, Q. Zhang, Y. Wang, D. Ma and L. Wang, *J. Mater. Chem. C*, 2019, **7**, 1014–1021.

20 Y. H. Chen, C. C. Lin, M. J. Huang, K. Hung, Y. C. Wu, W. C. Lin, R. W. Chen-Cheng, H. W. Lin and C. H. Cheng, *Chem. Sci.*, 2016, **7**, 4044–4051.

21 M. J. Sung, H. Chubachi, R. Sato, M.-K. Shin, S.-K. Kwon, Y.-J. Pu and Y.-H. Kim, *J. Mater. Chem. C*, 2017, **5**, 1090–1094.

22 T. Shan, Z. Gao, X. Tang, X. He, Y. Gao, J. Li, X. Sun, Y. Liu, H. Liu, B. Yang, P. Lu and Y. Ma, *Dyes Pigm.*, 2017, **142**, 189–197.

23 H. Lim, H. J. Cheon, G. S. Lee, M. Kim, Y. H. Kim and J. J. Kim, *ACS Appl. Mater. Interfaces*, 2019, **11**, 48121–48127.

24 X. Guo, P. Yuan, X. Qiao, D. Yang, Y. Dai, Q. Sun, A. Qin, B. Z. Tang and D. Ma, *Adv. Funct. Mater.*, 2020, **30**, 1908704.

25 C. Lin, P. Han, S. Xiao, F. Qu, J. Yao, X. Qiao, D. Yang, Y. Dai, Q. Sun, D. Hu, A. Qin, Y. Ma, B. Z. Tang and D. Ma, *Adv. Funct. Mater.*, 2021, **31**, 202106912.

26 Y. Luo, K. Zhang, Z. Ding, P. Chen, X. Peng, Y. Zhao, K. Chen, C. Li, X. Zheng, Y. Huang, X. Pu, Y. Liu, S.-J. Su, X. Hou and Z. Lu, *Nat. Commun.*, 2022, **13**, 6892.

27 T. Hatakeyama, K. Shiren, K. Nakajima, S. Nomura, S. Nakatsuka, K. Kinoshita, J. Ni, Y. Ono and T. Ikuta, *Adv. Mater.*, 2016, **28**, 2777–2781.

28 J. Lim, J. M. Kim and J. Y. Lee, *Adv. Mater.*, 2024, e2312774.

29 X. Wang, L. Wang, G. Meng, X. Zeng, D. Zhang and L. Duan, *Sci. Adv.*, 2023, **9**, eadh1434.

30 T. B. Nguyen, H. Nakanotani, C. Y. Chan, S. Kakumachi and C. Adachi, *ACS Appl. Mater. Interfaces*, 2023, **15**, 23557.

31 C. Kuang, S. Li, I. Murtaza, Z. Meng, H. Li, X. Zhang, C. Wu, K. N. Tong, Y. Shang, Y. He, Y. Zhu, G. Wei and H. Meng, *Small*, 2023, e2311114.

32 J. Park, K. J. Kim, J. Lim, T. Kim and J. Y. Lee, *Adv. Mater.*, 2022, **34**, 2108581.

33 X. Liang, Z. P. Yan, H. B. Han, Z. G. Wu, Y. X. Zheng, H. Meng, J. L. Zuo and W. Huang, *Angew. Chem.*, 2018, **57**, 11316–11320.

34 W. Cai, W. Li, X. Song, X. Zheng, H. Guo, C. Lin, D. Yang, D. Ma, M. Ng and M. C. Tang, *Adv. Sci.*, 2024, e2407278.

35 D. Yokoyama, *J. Mater. Chem. C*, 2011, **21**, 19187.